LANGMUIR

pubs.acs.org/Langmuir Article

Nanoscale Patterning of Surface Nanobubbles by Focused Ion Beam

Anayet Ullah Siddique, Rui Xie, Danielle Horlacher, and Roseanne Warren*



Cite This: Langmuir 2024, 40, 14613-14622



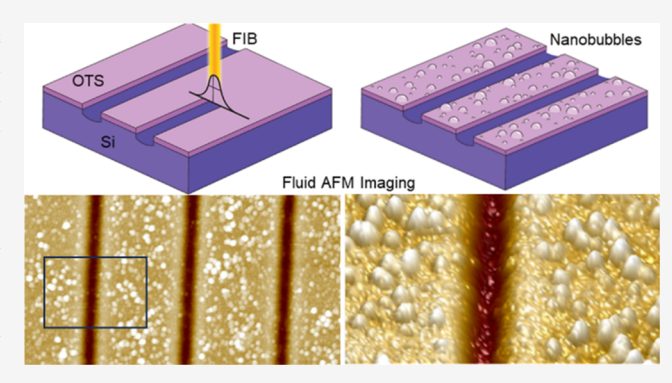
ACCESS

Metrics & More

Article Recommendations

Supporting Information

ABSTRACT: Surface nanobubbles forming on hydrophobic surfaces in water present an exciting opportunity as potential agents of top-down and bottom-up nanopatterning. The formation and characteristics of surface nanobubbles are strongly influenced by the physical and chemical properties of the substrate. In this study, focused ion beam (FIB) milling is used for the first time to spatially control the nucleation of surface nanobubbles with 75 nm precision. The spontaneous formation of nanobubbles on alternating lines of a self-assembled monolayer (octadecyltrichlorosilane) patterned by FIB is detected by atomic force microscopy. The effect of chemical vs topographical surface heterogeneity on the formation of nanobubbles is investigated by comparing samples with OTS coating applied pre- vs post-FIB patterning. The results



confirm that nanoscale FIB-based patterning can effectively control surface nanobubble position by means of chemical heterogeneity. The effect of FIB milling on nanobubble morphology and properties, including contact angle and gas oversaturation, is also reported. Molecular dynamics simulations provide further insight into the effects of FIB amorphization on surface nanobubble formation. Combined experimental and simulation investigations offer insights to guide future nanobubble-based patterning using FIB milling.

■ INTRODUCTION

Surface nanobubbles are nanoscale spherical-cap-shaped gaseous domains that form on various surfaces immersed in water. 1,2 To date, the properties and applications of surface nanobubbles nucleated on homogeneous substrates have been well-studied. Surface nanobubbles tend to form on hydrophobic surfaces, with some reports of nanobubbles on hydrophilic surfaces.^{3,4} Applications of surface nanobubbles explored to date include surface cleaning enhancement, 5,6 mineral flotation, wafer-scale graphene transfer, and manipulation of no-slip boundary conditions in microfluidic channels. While such applications demonstrate the utility of large-scale, uniform distributions of surface nanobubbles, equally intriguing are the potential applications of spatially confined nanobubbles. In particular, the ability to control surface nanobubble placement at sub-100 nm length scales opens the door to new methods of top-down/bottom-up nanoscale patterning using surface nanobubbles.

Several prior works have achieved spatial control of nanobubble formation using nanopatterned hydrophobic/hydrophilic surfaces. Agrawal et al. demonstrated the preferential nucleation of surface nanobubbles on the hydrophobic regions of poly(methyl methacrylate) (PMMA)—polystyrene (PS) block copolymer nanodomains. Hydrophobic—hydrophilic patterns for nanobubble positioning have also been achieved via electron beam-induced deposition (Teflon-carbon nanodomains), microcontact printing (octadecanethiol-*n*-octadecylphosphonic acid hydrophobic do-

mains), 12 and electron beam lithography (patterned PMMA films). 13 The ability of nanobubbles to serve as templates for bottom-up patterning has been demonstrated through, e.g., surface nanobubble-induced PS nanoindents, 14,15 NaCl solution evaporation around surface nanobubbles, 16 convective self-assembly of Au nanoparticles around nanobubbles and droplets, 17 and microporous Cu electrodeposition around bubble templates. 18

This work presents the first demonstration of sub-100 nm, top-down, spatial control of surface nanobubbles using focused ion beam (FIB) milling. FIB milling offers numerous advantages compared to previously demonstrated surface nanobubble patterning approaches, including (1) higher resolution, reduced proximity effects, and higher throughput vs electron beam lithography, ^{19,20} (2) direct-write patterning that avoids stamp fabrication, as in microcontact printing, and (3) precise placement of features unlike self-assembly based methods such as block copolymer lithography. There are, however, several noteworthy drawbacks of FIB milling that directly impact its compatibility with surface nanobubble patterning. In the process of ion beam exposure, FIB milling

Received: April 24, 2024 Revised: June 23, 2024 Accepted: June 24, 2024 Published: July 4, 2024





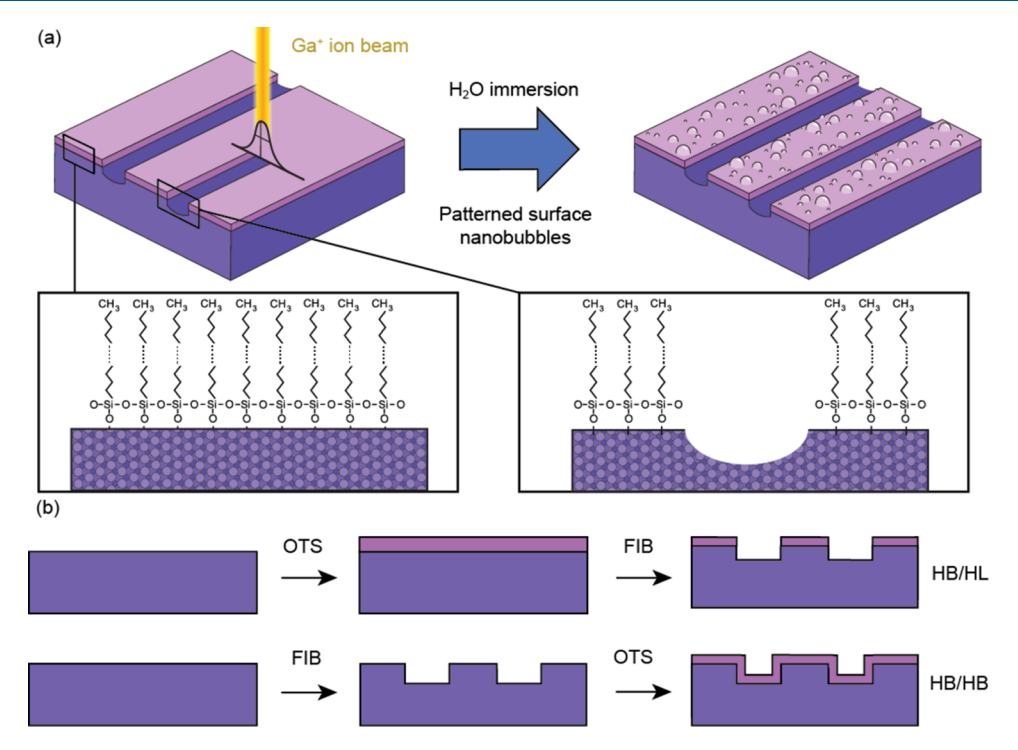


Figure 1. (a) Conceptual illustration of FIB-based patterning of surface nanobubbles. A hydrophobic SAM (OTS) is applied to a Si surface (left inset), patterned by FIB milling (right inset), and then immersed in water. (b) Process flow diagrams for the two types of nanostructured patterns: HB/HL (top) and HB/HB (bottom).

creates myriad changes to the underlying substrate, including amorphization of Si (including up to ~20 nm depth), ²¹ Ga⁺ ion implantation, ²² and changes in surface roughness. ²³ Molecular dynamics (MD) simulations have demonstrated changes in water contact angle, ²⁴ in addition to nano-order deformation and hillock structure formation. ²² Further complicating matters is the spatial gradient of such effects arising from the Gaussian beam shape, which spreads beyond the user-defined patterning region. ²⁵ As a result of these complex ion—surface interactions, an experimental demonstration is needed to validate the concept of nanoscale FIB-based patterning of surface nanobubbles and determine the limits of feature density, pattern resolution, and near-flat patterning ability.

Figure 1a provides an overview of the approach employed here to achieve surface nanobubble patterning using FIB milling. A Si surface is coated with the hydrophobic selfassembled monolayer (SAM) octadecyltrichlorosilane (OTS) (Figure 1a, left inset). Upon exposure to the FIB, the SAM is selectively removed from the substrate (Figure 1a, right inset). When immersed in water, surface nanobubbles are selectively formed in the SAM regions. FIB patterning can induce full or partial monolayer removal or degradation, depending on factors such as beam dose and current density. 26,27 Changes to the underlying Si surface, such as ion implantation and amorphization, are also expected. To distinguish FIB vs non-FIB regions by atomic force microscopy (AFM), it is necessary to provide some depth contrast to the line patterns. To separate ion beam exposure effects from topographical effects, two samples were made for comparison. The first sample follows the intended nanopatterning approach of OTS coating, followed by FIB milling (Figure 1b, top), and is referred to as "hydrophobic/hydrophilic" (HB/HL). The control sample was

FIB milled first, followed by OTS coating (Figure 1b, bottom), and is called "hydrophobic/hydrophobic" (HB/HB).

MATERIALS AND METHODS

Materials. OTS (95%) and toluene (anhydrous, 99.8%) were purchased from Fisher Scientific. Acetone (>99.9%) and ethanol (>99.8%) were purchased from Sigma-Aldrich. Chloroform (\geq 99% ACS Reagent grade) was purchased from Lab Alley. Ultrapure water (conductivity, 18.2 MΩ cm) was obtained from a Milli-Q system (Millipore Corporation, Boston, MA). To avoid contamination, all fluid handling was conducted using glass beakers and syringes cleaned with ethanol and ultrapure water before use. Before each experiment, the AFM liquid cell was rinsed with isopropyl alcohol, ethanol, and ultrapure water and dried with nitrogen gas.

Substrate Modification. OTS-modified silicon surfaces were prepared by first treating the silicon wafer with oxygen plasma for 2 min at 195 W. A 5 mM solution of OTS was prepared by dissolving OTS in toluene in a Class 1000 cleanroom environment. The silicon wafer was immersed in the OTS solution and kept in a sealed container for 24 h. Upon removal from the solution, the OTS-modified wafer was quickly rinsed with chloroform. The wafer was sonicated for 15 min each in chloroform, toluene, and acetone to remove unbound OTS molecules. The wafer was then dried under a stream of nitrogen gas and kept in a cleanroom for at least 24 h. Before each AFM experiment, all substrates were sonicated in toluene, acetone, and ethanol in turn for 5 min each and dried under a stream of nitrogen gas.

An FEI Helios NanoLab 650 focused ion beam scanning electron microscope was used to fabricate the nanostructures. NanoBuilder software was used to design the fabricated structures. Single-pixel lines of 20 μ m length and 75 nm width were milled using a voltage of 30 keV and an ion beam current of 24 pA. Additional line patterns were created with ion beam currents of 7, 30, and 40 pA at 30 keV, and 0.36 and 0.068 nA at 5 keV, to determine the effect of ion beam parameters on formed nanostructures. HB/HL surfaces were prepared by OTS coating followed by FIB milling of nanostructures (Figure 1b, top). HB/HB surfaces were prepared by FIB milling of nanostructures, followed by an OTS coating (Figure 1b, bottom).

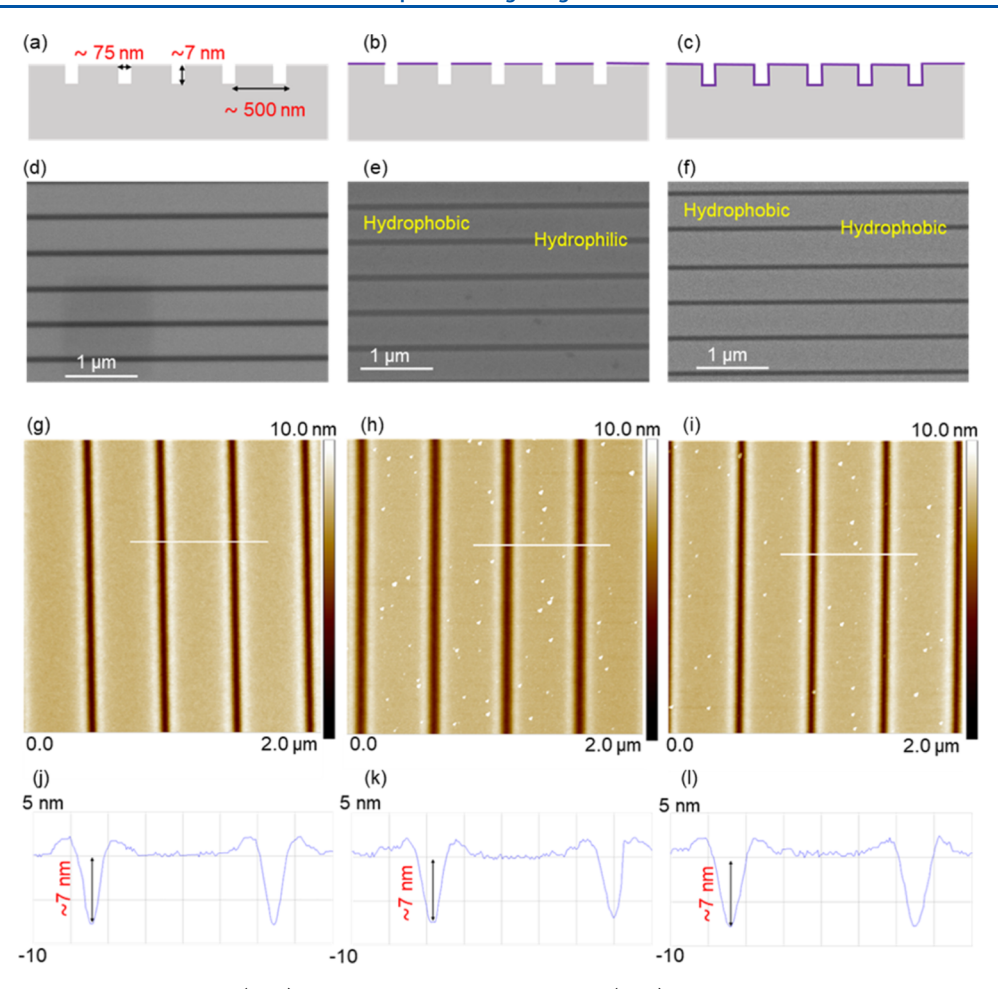


Figure 2. Schematic and SEM images of (a, d) uncoated Si after FIB milling, (b, e) HB/HL nanopatterned surface, and (c, f) HB/HB nanopatterned surface. Schematic diagrams indicate surface regions coated with the OTS (purple shading). AFM images of (g) FIB-milled uncoated Si, (h) HB/HL, and (i) HB/HB surfaces in air. (j-l) Cross-sectional AFM profiles of (g)-(i), respectively. Profiles are taken along the white lines drawn in (g)-(i).

AFM Experiments. AFM measurements were conducted using a Dimension Icon AFM instrument (Bruker). AFM experiments in air were performed using a silicon nitride cantilever (Bruker) with a nominal spring constant of 0.4 N/m and a tip radius of 2 nm. AFM experiments in fluid were performed using a silicon nitride cantilever (DNP-C, Bruker) with a nominal spring constant of 0.24 N/m and a tip radius of 20 nm. ScanAsyst mode was used in both air and fluid experiments.

Before each fluid experiment, the AFM liquid cell was rinsed with isopropyl alcohol, ethanol, and ultrapure water and dried with nitrogen gas. The fluid cell was first mounted with the AFM head (scanner) and sealed with a translucent silicone O-ring. A drop of Milli-Q water was then added directly to the sample substrate using a glass syringe, and another drop was placed in the liquid cell. When the optical head was lowered, the two droplets coalesced and were squeezed to form a meniscus between the substrate and the liquid cell. Prior to beginning of the experiments, the system was left for 30 min to reach thermal equilibrium. All AFM experiments were performed at room temperature. Typical scan areas were 2 μ m × 2 μ m, and the scan time for each image was approximately 8–9 min. Bruker NanoScope Analysis 2.0 software was used for AFM image processing.

Degassed Experiments. Degassed fluid AFM experiments were performed using DI water placed inside a desiccator at room temperature for 24 h under reduced pressure. The time between the degassed water being removed from the desiccator and being injected into the fluid cell was kept as short as possible. The 30 min equilibration time before imaging was bypassed in degassed experiments.

Contact Angle Measurement. The water contact angle was measured using a contact angle goniometer (model no. 100-00-115, ramé-hart instrument co.). The contact angles of water on the bare silicon wafer and hydrophobized flat OTS-coated silicon wafer were measured by the sessile drop method. Each measurement was repeated at least five times at different surface locations for each substrate, and the average result was reported.

MD Simulations. MD simulations were implemented in Largescale Atomic/Molecular Massively Parallel Simulator (LAMMPS). The size of the system was approximately $15 \text{ nm} \times 4.5 \text{ nm} \times 25 \text{ nm}$ in the x, y, and z directions, respectively. The potential for surface preparations was the three-body Tersoff potential. The substrate was first annealed at 2000 K with NVT ensemble for 2 ns, then relaxed at 2000 K with NVE ensemble for another 2 ns, and then quenched to 300 K at a rate of 10^{12} K/s. Periodic boundary conditions were applied in the x, y, and z directions for this step.

After the amorphous substrate was prepared, an extended simple point charge (SPC/E) water model with fixed bond lengths and angles was prepared. Water molecules were separated 3.1 Å from each other and mixed with 1.4% nitrogen molecules at least 1 Å above the substrate as the initial configuration. Periodic boundary conditions were applied in the x and y directions, and the mirror boundary condition was applied in the z direction.

Nanobubble simulations were implemented using the canonical (NVT) ensemble, with temperature controlled by the Nose–Hoover thermostat at 300 K and a time step of 1 fs. Long-range Coulombic interactions were calculated by the particle–particle particle–mesh (PPPM) method. The Lennard-Jones (LJ) potential with a cutoff

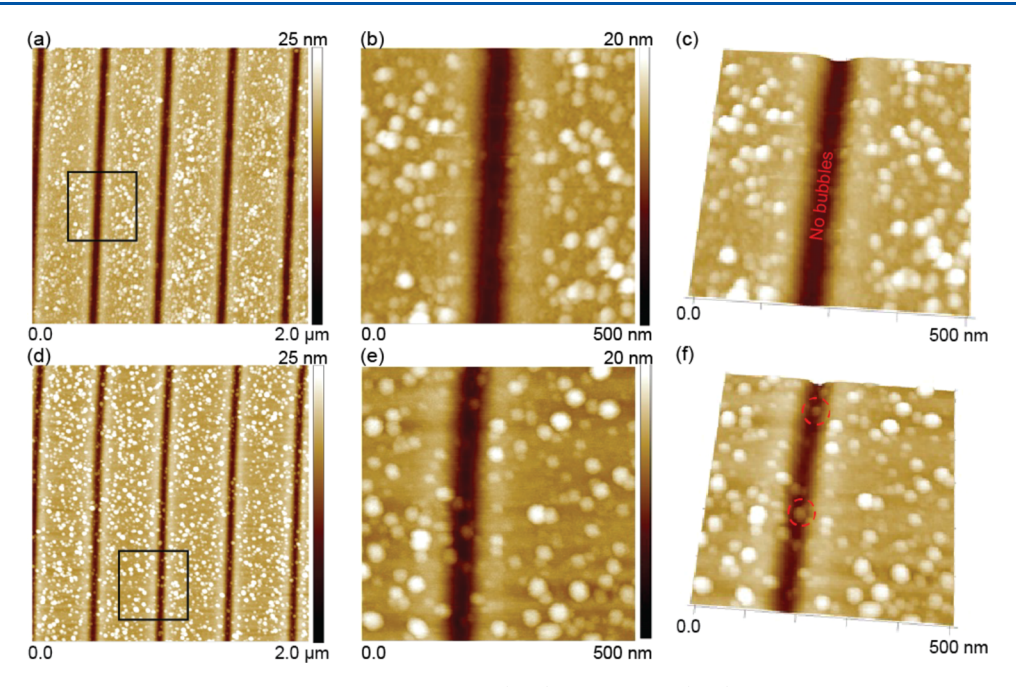


Figure 3. Fluid AFM measurements of nanobubbles formed on HB/HL (a–c) and HB/HB (d–f) surfaces. AFM height images of nanobubbles on HB/HL (a) and HB/HB (d) surfaces, with a scan size of 2 μ m × 2 μ m. Zoomed-in images of a single HB/HL (b) or HB/HB (e) trench with a scan size of 500 nm × 500 nm. 3D images of nanobubbles on HB/HL (c) and HB/HB (f) substrates of the same areas selected in (b) and (e). No bubbles formed inside the hydrophilic trench of the HB/HL surface (c). The nanobubbles formed inside the trench of the HB/HB surface can be seen clearly (red circle) (f).

value of 12 Å was applied for the van der Waals interaction. Lorentz—Berthelot mixing rules were applied if the species were different, and LJ potential parameters were obtained from refs 24 and 28–31.

■ RESULTS AND DISCUSSION

Characterization of Nanopatterned Surfaces. Figure 2 provides schematic (Figure 2a-c), scanning electron microscopy (SEM) (Figure 2d-f), and AFM (Figure 2g-l) images of nanostructured surfaces fabricated via FIB milling. In Figure 2d, the Si surface is uncoated (no OTS layer) and displays a regular pattern of trenches of width 75 nm and period 500 nm. Figure 2e provides an SEM image of the HB/HL surface in which FIB milling was completed after the OTS coating. Figure 2f provides an SEM image of the HB/HB surface prepared by OTS coating after FIB milling. The line width and period of the FIB-milled trenches are consistent across all three surfaces (uncoated, HB/HL, and HB/HB), indicating no significant shrinkage of line width occurs with the OTS layer. In all cases, the FIB-milled nanopatterned surfaces are regular and uniform across the surface.

Figure 2g–l provides AFM images of uncoated Si, HB/HL, and HB/HB nanopatterns in air. While the uncoated Si surface is clear (Figure 2g), small particles are visible on the OTS-modified surfaces (Figure 2h,i). These particles may be caused by small amounts of OTS aggregation during coating. AFM cross sections (Figure 2j–l) confirm that the depth of the trenches is ~7 nm for uncoated, HB/HL, and HB/HB surfaces. The trench width of 75 nm is unaffected by the OTS coating and remains consistent for uncoated, HB/HL, and HB/HB surfaces. A step height of ~7 nm was chosen to differentiate between hydrophobic and hydrophilic regions during fluid-cell AFM imaging. A trench width of 75 nm was chosen so that the fluid-cell AFM tip (~20 nm radius) could completely enter the trenches. If the trenches are smaller than the AFM tip, the nanopatterns may reflect the shape of the tip

rather than the geometry of the patterns. If the trench width is larger than 75 nm, it will result in a higher depth or step height for HB/HL and HB/HB surfaces, as discussed in Effect of Ion Beam Parameters on Nanobubble Formation and Patterning section. A higher trench depth impedes the ability to measure surface nanobubble features by fluid AFM on both upper and lower regions of nanopatterned surfaces within the same scan area.

Unpatterned OTS on Si has a measured water drop contact angle of 110 \pm 2 vs 36 \pm 1° for pure Si. The measurement confirms that the HB/HL surface provides both chemical and topographical surface heterogeneities, while the HB/HB surface provides only topographical surface heterogeneity.

Fluid AFM Imaging. Fluid AFM imaging was first conducted on a planar OTS-modified Si substrate to measure the properties of surface nanobubbles formed when a water droplet contacts the hydrophobic surface (Figure S1). The AFM height image (Figure S1a) shows the presence of dense, randomly located features on the OTS-coated surface. Line scans of these features indicate bubble-like profiles of a typical height of approximately 10 nm and width of approximately 50 nm (Figure S1b,c). To confirm these features are bubbles and not artifacts of surface preparation or imaging, we performed degassed fluid AFM experiments. The results confirm that the features are indeed bubbles, appearing on the OTS-Si only in the presence of dissolved gas, with no surface features visible in the degassed experiment (Figure S2).

Fluid AFM imaging was then conducted on HB/HL and HB/HB nanopatterned substrates to investigate the presence of nanobubbles on the surfaces vs in the trenches of both samples (Figure 3). In the case of HB/HL patterns, surface nanobubbles are visible on the upper hydrophobic stripes but not in the hydrophilic trenches (Figure 3a–c). For the HB/HB patterns, nanobubbles formed both on the upper stripes and within the grooves between the stripes (Figure 3d–f). Line

scans of HB/HL and HB/HB samples (Figure S3) indicate comparable height profiles for bubbles located on the hydrophobic regions of the HB/HL and HB/HB surfaces. The features are also analogous to bubble shapes indicated in line scans of unpatterned OTS (Figure S1b,c).

Table 1 quantifies the presence vs absence of nanobubbles in HB/HB vs HB/HL trenches by comparing "AFM feature

Table 1. AFM Feature Density for HB/HL and HB/HB Patterns

	HB/HL (number/ μ m ²)	HB/HB (number/ μ m ²)	
trenches	3.3	20.0	
stripes	18.2	21.2	

density" counts for both samples. While the fluid AFM tip is able to scan within the full width of the trenches, it is not possible to obtain accurate values of surface nanobubble density within the trenches due to uncertainties distinguishing individual bubble features within the trenches. A given AFM feature, for example, may consist of one or several bubbles that cannot be resolved with confidence. Feature density counts provided in Table 1 are based on Figure 3a,d fluid AFM images. The results indicate a clear absence of nanobubbles in HB/HL trenches compared to HB/HB trenches and HB/HL or HB/HB upper stripes. Assuming similar errors in using "AFM feature density" as a proxy for surface nanobubble density in both samples, there is an approximately 83% reduction in bubble feature density for HB/HL surfaces in

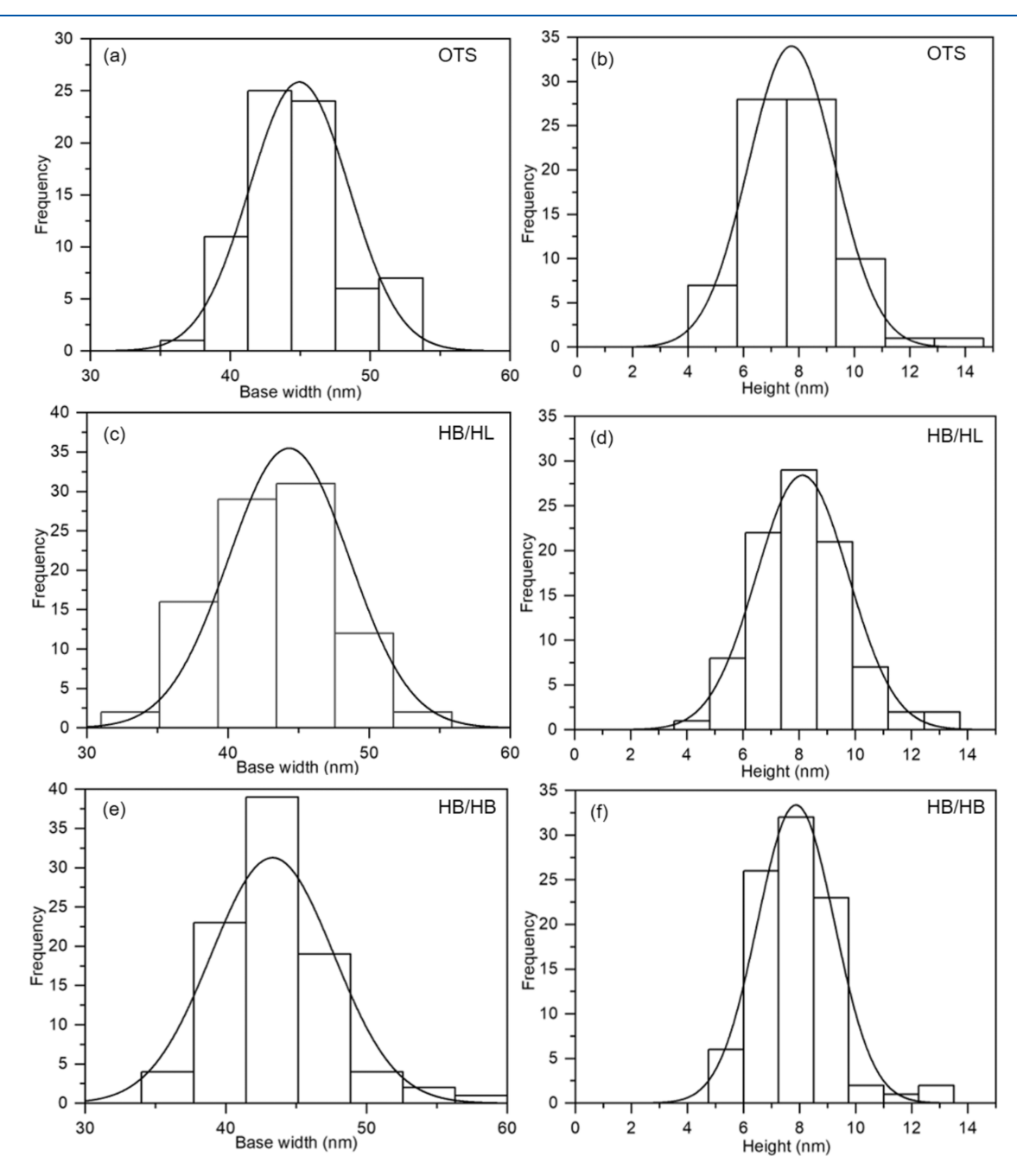


Figure 4. Base width (a, c, e) and height (b, d, f) histograms of nanobubbles on flat OTS (a, b), HB/HL (c, d), and HB/HB (e, f) surfaces. Histograms are fit with Gaussian curves.

FIB-milled areas. The results demonstrate the ability to control the placement of surface nanobubbles using chemical heterogeneity achieved by FIB milling of OTS.

Nanobubble Properties. The morphology of nanobubbles present on HB/HL vs HB/HB vs unpatterned OTS surfaces was quantified by comparing the bubble height (H) and base width (L). Figure 4 presents height and base width histograms fit with Gaussian distributions for unpatterned OTS (Figure 4a,b), HB/HL (Figure 4c,d), and HB/HB (Figure 4e,f) surfaces. The mean height, mean width, size range, and standard deviation are summarized in Table 2. Due to

Table 2. Statistical Table of the Size of Nanobubbles Formed on Different Surfaces

geometric parameters		flat OTS	HB/HL	HB/HB
width, L (nm)	mean	45.1	44.315	43.32
	range	38-59	34-55	35-59
	standard deviation	3.873	4.263	4.33
height, H (nm)	mean	7.731	8.116	7.8696
	range	4.57 - 13.1	4.08 - 12.83	5.07-13.1
	standard deviation	1.553	1.635	1.367

uncertainties in obtaining exact lateral dimensions of nanobubbles formed within trenches, height and width values are reported for bubble features present along upper surface stripes only. The histograms indicate similar morphologies for nanobubbles on plain OTS vs HB/HL and HB/HB patterned substrates.

Statistical analysis was performed to test for significant differences in height and width between bubbles formed on flat OTS surfaces vs nanopatterned surfaces (HB/HL and HB/HB). A paired sample t test was used with a significance level (p-value) of 0.05. The average widths of the nanobubbles on the HB/HL and HB/HB substrates were 44.32 and 43.32 nm, respectively, which were not significantly different (p > 0.05) from the average width of the nanobubbles on unpatterned OTS (mean = 45.10 nm). No significant difference (p > 0.05) was observed between the heights of nanobubbles on HB/HL (mean = 8.12 nm) vs unpatterned OTS (mean = 7.75 nm) or those of nanobubbles on HB/HB (mean = 7.87 nm) vs unpatterned OTS.

Outcomes of this morphology comparison indicate that there is no measurable change in the HB regions of the OTS coating as a result of the FIB milling process. With the ion beam current (24 pA) and voltage (30 keV) employed here, the OTS layer is effectively removed within the 75 nm line width of the HL regions without altering adjacent monolayer properties. The validity of this conclusion under other FIB milling conditions is explored in Effect of Ion Beam Parameters on Nanobubble Formation and Patterning section.

Additional nanobubble properties of interest include the contact angle vs height and the equilibrium contact angle ($\theta_{\rm e}$). Figure 5a plots the relationship between the contact angle (θ) and the height of nanobubbles measured on HB/HL and HB/HB surfaces, with θ approximated by eq 1

$$\theta = \tan^{-1} \left(\frac{2H}{L} \right) \tag{1}$$

Nanobubbles produced on HB/HL and HB/HB surfaces have contact angles in the range of 13.4–28.5 and 16–25.5°, respectively, with a combined average contact angle of 20°. The increase in contact angle with height shown in Figure 5a is consistent with previous nanobubble reports. Differences in height, width, and contact angle for flat OTS, HB/HL, and HB/HB nanobubbles vs literature reports for OTS surfaces are likely due to differences in bubble formation methods, i.e., lower dissolved gas content in the water droplet method employed here vs fluid exchange or temperature difference methods. The surface of the surfac

The relationship between gas saturation, ζ , and the equilibrium contact angle can be evaluated using the Lohse–Zhang theory^{35,36} described by eq 2

$$\zeta = \frac{4\sigma}{P_{\text{atm}}L} \sin \theta_e \tag{2}$$

where σ is the air–liquid surface tension (0.072 N/m) and $P_{\rm atm}$ is the atmospheric pressure. Figure 5b plots $\sin\theta$ vs L for HB/HB and HB/HL nanobubbles. According to eq 2, gas saturation can be calculated from a linear fit of $\sin\theta/L$. The calculated ζ value corresponds to an air saturation of $\zeta=8.2$, which is plausible and in line with the value predicted by the Lohse–Zhang theory. According to the theory, nanobubbles must be sustained by saturation of at least $\zeta\approx4-7$, 36,37 which indicates that gas saturation is a key factor for the formation of surface nanobubbles on HB/HL and HB/HB surfaces.

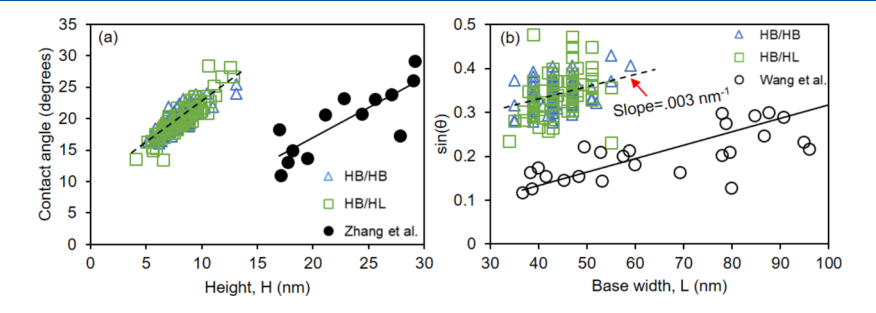


Figure 5. (a) Linear dependence of contact angle vs height of nanobubbles on HB/HL and HB/HB surfaces. Data from Zhang et al. shows a similar trend for contact angle vs height of nanobubbles. The dashed line is fitted from our experimental data, and the solid line is fitted from Zhang et al. Adapted with permission from Zhang et al., Soft Matter 2010, 6(18), 4515-4519. Copyright 2010 Royal Society of Chemistry. (b) $\sin \theta$ vs nanobubble width L for HB/HL and HB/HB surfaces. The dashed line is fitted to our experimental data. The slope of 0.003 nm⁻¹ corresponds to a gas saturation of $\zeta = 8.2$. Data from experiments by Wang et al. so n nanostructured surfaces is fitted with a solid line. The solid line corresponds to a slope of 0029 nm⁻¹ and a gas saturation of $\zeta = 8.2$. Adapted with permission from Wang et al., Soft Matter 2017, 13(32), 5381–5388. Copyright 2017 Royal Society of Chemistry.

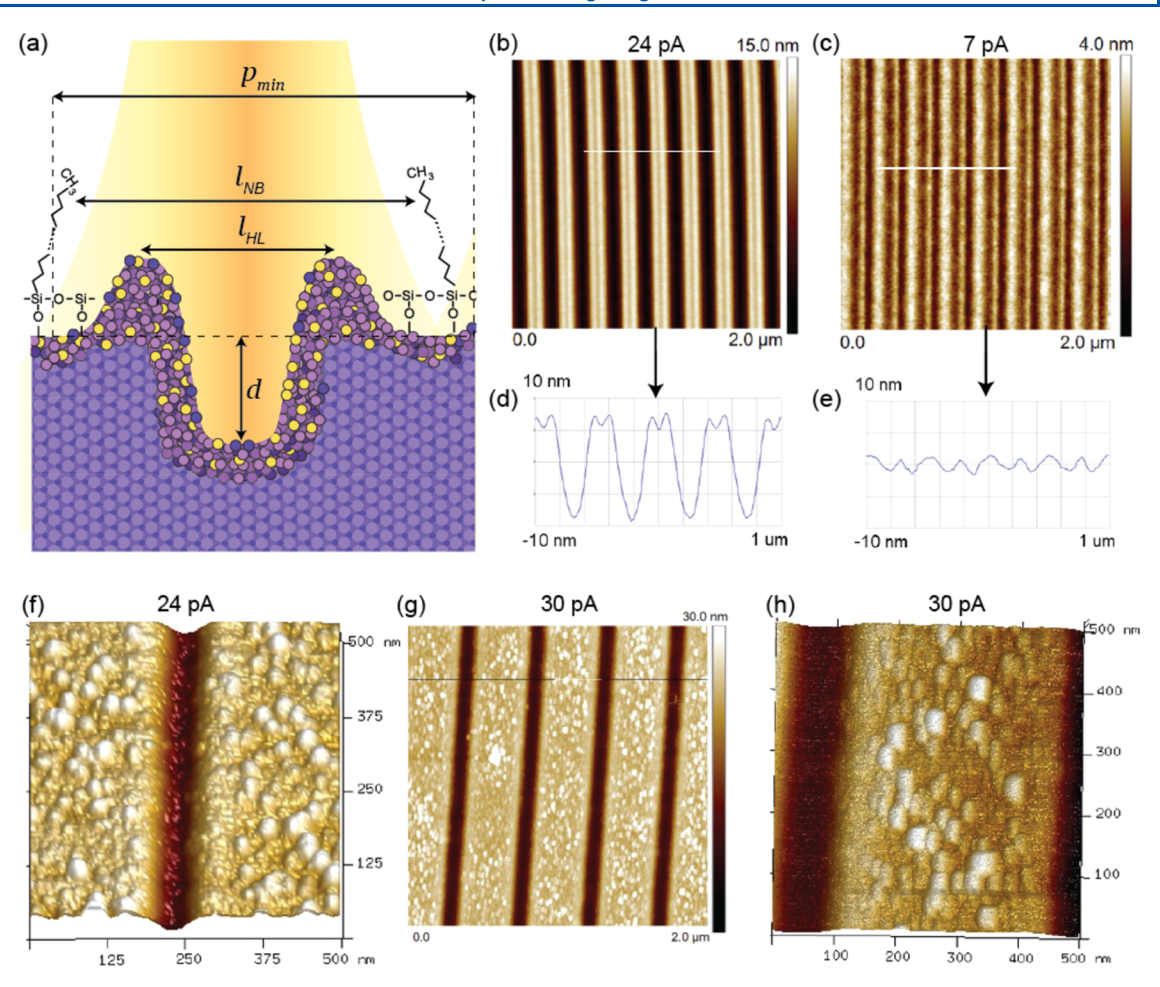


Figure 6. (a) Conceptual illustration of FIB interactions with OTS-Si for surface nanobubble patterning. Nanobubble pitch resolution, p_{\min} , is limited by proximity effects. Coulomb scattering causes beam interaction with OTS molecules adjacent to HL features, resulting in $l_{\rm NB} \geq l_{\rm HL}$. The coupled nature of d and $l_{\rm HL}$ affects near-flat patterning abilities with FIB. (b, c) AFM images of HB/HL patterns with 250 nm period at 24 (b) and 7 pA (c) beam currents. (d, e) Cross-sectional AFM profiles of (b) and (c), respectively. Fluid AFM images of nanobubbles formed on HB/HL surfaces patterned at 24 pA (f) vs 30 pA (g, h). HB/HL surfaces patterned at 30 pA show an absence of nanobubbles in HB regions adjacent to FIB-patterned trenches.

Effect of Ion Beam Parameters on Nanobubble Formation and Patterning. The above experimental results demonstrate the concept of nanobubble patterning using FIB removal of OTS. The results were obtained with a FIB accelerating voltage of 30 keV, a beam current of 24 pA, and a pitch of 500 nm for alternating HB/HL lines, producing an HL trench width of 75 nm and a depth of 7 nm. We now investigate the effects of FIB milling parameters on surface nanobubble patterning outcomes. Nonidealities such as Si amorphization, proximity effects, and extended SAM removal due to Coulomb scattering are dependent on the beam current, beam accelerating voltage, and pattern density. These factors will affect surface nanobubble patterning feature resolution (l_{NB}) , pitch resolution (p_{min}) , and pattern depth (d) (Figure 6a). Results of particular note are (1) limitations on minimum pitch resolution due to proximity effects, (2) the effects of beam spread on nanobubble vs trench feature resolution (l_{NB} vs $l_{\rm HL}$), and (3) interrelationships between d and $l_{\rm HL}$ that are unique to FIB nanobubble patterning.

Pitch resolution and feature density were explored by reducing the period of HB/HL features from 500 nm (Figure 2) to 250 nm (Figure 6b–e). At 30 keV accelerating voltage and 24 pA beam current (Figure 6b,d), proximity effects at 250 nm period become significant. This can be seen in the double

hillock structure present in cross-sectional AFM scans of the HB regions (Figure 6d). Due to the smaller period, amorphization effects nearly overlap at 24 pA beam current, and instead of flat HB regions we observe irregular/uneven stripes. To reduce proximity effects, the beam current was lowered from 24 to 7 pA. At 7 pA beam current and 250 nm period, HL regions are not created properly, and the nanopatterned surface has no defined stripes/lines (Figure 6c,e). The results indicate that a minimum pitch resolution $p_{\min} > 250$ nm is required with the optimum beam parameters of 30 keV and 24 pA. Increasing the HB/HL pitch reduces interactions between adjacent patterns, and surface nanobubble patterns with larger periods (e.g., 1000 nm) are observed to be similar to patterns with a 500 nm period.

With FIB patterning of nanobubbles, the minimum feature size of the HL regions $(l_{\rm HL})$ as measured by AFM in air may differ from the minimum feature size manifested in the nanobubble pattern $(l_{\rm NB})$. The extent of this difference is a function of the FIB milling parameters, as illustrated in the fluid AFM results in Figure 6f—h. Figure 6f provides a high-resolution fluid AFM image of surface nanobubbles patterned with 30 keV accelerating voltage, 24 pA beam current, and 500 nm period. In this high-resolution scan, surface nanobubbles are visible up to the boundaries of the HB/HL regions. In this

case, HB/HL and nanobubble patterning resolution are approximately equal, e.g., $l_{\rm HL}=l_{\rm NB}=75$ nm. When the beam current is increased to 30 pA, the HL trench width increases from $l_{\rm HL}=75$ to 90 nm, as measured by AFM in air. Upon exposure of the surface to DI water (Figure 6g,h), there is a notable absence of nanobubbles in both the trenches and the HB regions immediately adjacent to HL regions (Figure 6h). At 30 pA, Coulomb scattering induces greater beam spread that affects the OTS structure in HB regions next to HL regions enough to change nanobubble formation in these areas. In this case, $l_{\rm NB} > l_{\rm HL}$, with an approximate value of $l_{\rm NB} \sim 150$ nm. The distribution of nanobubbles along the central regions of the HB stripes at 30 pA is similar to the distribution observed with the 24 pA HB/HL surface.

With FIB-based patterning of surface nanobubbles, there is a complex relationship between the feature size, $l_{\rm NB}$, and the feature depth, d. As an example, Figure S4 considers the case of increasing the width of HL regions by changing the beam current or the number of beam passes. In both cases, l_{NB} and d are coupled such that changing the HL region width changes the depth contrast between HB and HL regions, e.g., 75 nm width/7 nm depth with 24 pA beam current (Figure S4a,d) vs 105 nm width/18 nm depth with 40 pA single-pass beam current (Figure S4b,e) vs 115 nm width/32 nm depth with 40 pA double-pass beam current (Figure S4c,f). During fluid AFM imaging, the problem with a larger width and depth to the trenches is that the AFM tip cannot simultaneously provide an image of the inside of the trenches and the stripes. Moreover, there is a chance of false engagement, and there is no clear image of the nanobubbles that tend to form inside the trenches. With high aspect ratio features, a conical AFM tip is more effective than a pyramidal or tetrahedral AFM tip in resolving the actual profile of the surface; however, a sharp AFM probe tip will deform the soft nanobubbles. Increasing the beam current and/or dose also changes the surface morphology at the boundaries of the trenches (HB regions immediately adjacent to the HL regions) due to Si amorphization (Figure S4d-f). Surface swelling on the sides of the trenches is a limitation of FIB-based patterning of nanobubbles as it disrupts near-flat patterning abilities. The FIB accelerating voltage was reduced from 30 to 5 keV in an attempt to pattern HB/HL regions while minimizing beam interaction with the underlying Si (milling and amorphization). SEM images and AFM scans of the resulting patterns show a high degree of surface charging, large surface roughness, and poorly defined patterns, indicating that the OTS SAM is not fully removed from the surface at a low accelerating voltage.

Effect of Amorphization on Nanobubble Formation on Si. During FIB patterning, crystalline Si is converted to amorphous Si to a depth of several tens of nm. 21 To confirm that there is no tendency toward bubble formation in the HL regions (bare amorphous Si) and to better understand nanobubble formation at the molecular level on the stripes (OTS-Si), MD simulations were performed on HB/HL nanopatterned and amorphous Si surfaces (Figure 7). Amorphous Si substrates are designated "(100) amorphous" in Figure 7 based on the starting single-crystal orientation used to form the amorphous phase in the simulations. For 1.4% N_2 concentration, nanobubbles form in the OTS regions, but there are no bubbles in the amorphous Si region after 4 ns, matching experimental results. Isolated amorphous Si simulations confirm that N₂ accumulation near the surface does not lead to bubble formation (Figure 7b). In experiments, the

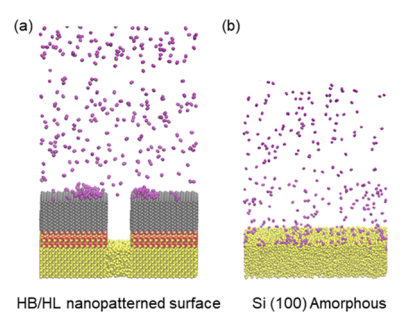


Figure 7. (a) MD simulations showing the nanobubble formation process on an HB/HL nanopatterned surface, with results matching the experiment (purple = N; yellow = Si; red = O; gray = OTS; H_2O molecules are not shown). (b) MD simulation of an isolated amorphous Si surface showing surface nanobubbles' inability to form. Simulations were run for 4 ns.

number percentage of nitrogen molecules is much less than $1.4\%~N_2$. We therefore conclude that the FIB milling process will not produce a Si surface conducive to nanobubble formation at typical dissolved gas quantities in the HL regions. This confirms the feasibility of FIB-based patterning to selectively define nanobubble and nanobubble-free regions on a Si substrate. Figure S5 and Table S1 provide information on additional scenarios evaluated through the simulations.

CONCLUSIONS

Experimental and simulation results presented in this work support the concept of top-down positioning of surface nanobubbles via FIB patterning. Using a minimal step height (7 nm) to distinguish between nanopatterned regions of the substrate, fluid AFM could identify the presence of alternating lines of 75 nm width displaying the presence and absence of surface nanobubbles. Degassed experiments confirm the features to be surface nanobubbles. When OTS was applied post-FIB milling, nanobubbles were detected across the whole substrate. These results confirm that nanobubbles were selectively placed on hydrophobic stripes but not on the surrounding hydrophilic trenches due to chemical heterogeneity and not topography. With predesigned hydrophobicity, the periodic striped nanostructured surface generated by FIB patterning can effectively regulate the position of surface nanobubbles with nanoscale control of bubble position. Careful selection of FIB milling parameters is required to ensure optimum control over nanobubble pitch resolution, nanobubble positioning resolution, and near-flat patterning capabilities using this approach.

ASSOCIATED CONTENT

Supporting Information

The Supporting Information is available free of charge at https://pubs.acs.org/doi/10.1021/acs.langmuir.4c01534.

Fluid AFM imaging of planar OTS-Si, degassed experiments, height profiles of nanobubbles formed on nanostructured surfaces, sectional analysis of nanopatterned surfaces fabricated by varying beam parameters, and additional MD simulation results (PDF)

AUTHOR INFORMATION

Corresponding Author

Roseanne Warren – Department of Mechanical Engineering, University of Utah, Salt Lake City, Utah 84112, United States; orcid.org/0000-0002-0520-8906; Email: roseanne.warren@utah.edu

Authors

Anayet Ullah Siddique — Department of Mechanical Engineering, University of Utah, Salt Lake City, Utah 84112, United States; orcid.org/0000-0001-9537-4299

Rui Xie – Department of Mechanical Engineering, University of Utah, Salt Lake City, Utah 84112, United States

Danielle Horlacher — Department of Mechanical Engineering, University of Utah, Salt Lake City, Utah 84112, United States; orcid.org/0009-0005-5372-1260

Complete contact information is available at: https://pubs.acs.org/10.1021/acs.langmuir.4c01534

Notes

The authors declare no competing financial interest.

ACKNOWLEDGMENTS

This work was supported in-part by NSF Award #1943907 and the University of Utah Department of Mechanical Engineering. The authors would like to thank the University of Utah's Electron Microscopy and Surface Analysis Lab and Utah Nanofab, which made this work possible.

REFERENCES

- (1) Lou, S.-T.; Ouyang, Z.-Q.; Zhang, Y.; Li, X.-J.; Hu, J.; Li, M.-Q.; Yang, F.-J. Nanobubbles on Solid Surface Imaged by Atomic Force Microscopy. *J. Vac. Sci. Technol., B: Microelectron. Nanometer Struct.*—*Process., Meas., Phenom.* **2000**, *18* (5), 2573–2575.
- (2) Ishida, N.; Inoue, T.; Miyahara, M.; Higashitani, K. Nano Bubbles on a Hydrophobic Surface in Water Observed by Tapping-Mode Atomic Force Microscopy. *Langmuir* **2000**, *16* (16), 6377–6380.
- (3) Zhang, X. H.; Zhang, X. D.; Lou, S. T.; Zhang, Z. X.; Sun, J. L.; Hu, J. Degassing and Temperature Effects on the Formation of Nanobubbles at the Mica/Water Interface. *Langmuir* **2004**, *20* (9), 3813–3815.
- (4) Ding, S.; Xing, Y.; Zheng, X.; Zhang, Y.; Cao, Y.; Gui, X. New Insights into the Role of Surface Nanobubbles in Bubble-Particle Detachment. *Langmuir* **2020**, *36* (16), 4339–4346.
- (5) Liu, G.; Craig, V. S. J. Improved Cleaning of Hydrophilic Protein-Coated Surfaces Using the Combination of Nanobubbles and SDS. ACS Appl. Mater. Interfaces 2009, 1 (2), 481–487.
- (6) Wu, Z.; Chen, H.; Dong, Y.; Mao, H.; Sun, J.; Chen, S.; Craig, V. S. J.; Hu, J. Cleaning Using Nanobubbles: Defouling by Electrochemical Generation of Bubbles. *J. Colloid Interface Sci.* **2008**, 328 (1), 10–14.
- (7) Sobhy, A.; Tao, D. Nanobubble Column Flotation of Fine Coal Particles and Associated Fundamentals. *Int. J. Miner. Process.* **2013**, 124, 109–116.
- (8) Gao, L.; Ni, G.-X.; Liu, Y.; Liu, B.; Castro Neto, A. H.; Loh, K. P. Face-to-Face Transfer of Wafer-Scale Graphene Films. *Nature* **2014**, 505 (7482), 190–194.
- (9) Wang, Y.; Bhushan, B. Boundary Slip and Nanobubble Study in Micro/Nanofluidics Using Atomic Force Microscopy. *Soft Matter* **2010**, *6* (1), 29–66.
- (10) Agrawal, A.; Park, J.; Ryu, D. Y.; Hammond, P. T.; Russell, T. P.; McKinley, G. H. Controlling the Location and Spatial Extent of Nanobubbles Using Hydrophobically Nanopatterned Surfaces. *Nano Lett.* **2005**, *5* (9), 1751–1756.
- (11) Nishiyama, T.; Takahashi, K.; Ikuta, T.; Yamada, Y.; Takata, Y. Hydrophilic Domains Enhance Nanobubble Stability. *ChemPhysChem* **2016**, *17* (10), 1500–1504.
- (12) Belova, V.; Shchukin, D. G.; Gorin, D. A.; Kopyshev, A.; Möhwald, H. A New Approach to Nucleation of Cavitation Bubbles at

- Chemically Modified Surfaces. Phys. Chem. Chem. Phys. 2011, 13 (17), 8015.
- (13) Wang, L.; Wang, X.; Wang, L.; Hu, J.; Wang, C. L.; Zhao, B.; Zhang, X.; Tai, R.; He, M.; Chen, L.; Zhang, L. Formation of Surface Nanobubbles on Nanostructured Substrates. *Nanoscale* **2017**, *9* (3), 1078–1086.
- (14) Wang, Y.; Bhushan, B.; Zhao, X. Nanoindents Produced by Nanobubbles on Ultrathin Polystyrene Films in Water. *Nanotechnology* **2009**, *20* (4), No. 045301.
- (15) Tarábková, H.; Janda, P. Nanobubble Assisted Nanopatterning Utilized for *Ex Situ* Identification of Surface Nanobubbles. *J. Phys.: Condens. Matter* **2013**, 25 (18), No. 184001.
- (16) Berkelaar, R. P.; Zandvliet, H. J. W.; Lohse, D. Covering Surface Nanobubbles with a NaCl Nanoblanket. *Langmuir* **2013**, 29 (36), 11337–11343.
- (17) Darwich, S.; Mougin, K.; Vidal, L.; Gnecco, E.; Haidara, H. Nanobubble and Nanodroplet Template Growth of Particle Nanorings versus Nanoholes in Drying Nanofluids and Polymer Films. *Nanoscale* **2011**, 3 (3), 1211.
- (18) Li, Y.; Jia, W.-Z.; Song, Y.-Y.; Xia, X.-H. Superhydrophobicity of 3D Porous Copper Films Prepared Using the Hydrogen Bubble Dynamic Template. *Chem. Mater.* **2007**, *19* (23), 5758–5764.
- (19) Nayfeh, M. Manipulation and Patterning of Surfaces (Nanolithography). Fundamentals and Applications of Nano Silicon in Plasmonics and Fullerines; Elsevier, 2018; pp 89–137.
- (20) Lawson, R. A.; Robinson, A. P. G. Overview of Materials and Processes for Lithography. *Frontiers of Nanoscience*; Elsevier, 2016; Vol. 11, pp 1–90.
- (21) Rumyantsev, A. V.; Borgardt, N. I.; Prikhodko, A. S.; Chaplygin, Y. A. Characterizing Interface Structure between Crystalline and Ion Bombarded Silicon by Transmission Electron Microscopy and Molecular Dynamics Simulations. *Appl. Surf. Sci.* **2021**, *540*, No. 148278.
- (22) Satake, S.; Ono, K.; Shibahara, M.; Taniguchi, J. Molecular Dynamics Simulation of Ga+ Ion Collision Process. *Nucl. Instrum. Methods Phys. Res., Sect. B* **2013**, 307, 235–239.
- (23) Ageev, O. A.; Kolomiytsev, A. S.; Konoplev, B. G. Formation of Nanosize Structures on a Silicon Substrate by Method of Focused Ion Beams. *Semiconductors* **2011**, *45* (13), 1709–1712.
- (24) Ozcelik, H. G.; Ozdemir, A. C.; Kim, B.; Barisik, M. Wetting of Single Crystalline and Amorphous Silicon Surfaces: Effective Range of Intermolecular Forces for Wetting. *Mol. Simul.* **2020**, *46* (3), 224–234
- (25) Lehrer, C.; Frey, L.; Petersen, S.; Ryssel, H. Limitations of Focused Ion Beam Nanomachining. J. Vac. Sci. Technol., B: Microelectron. Nanometer Struct.—Process., Meas., Phenom. 2001, 19 (6), 2533.
- (26) Yamada, Y.; Takahashi, K.; Ikuta, T.; Nishiyama, T.; Takata, Y.; Ma, W.; Takahara, A. Tuning Surface Wettability at the Submicron-Scale: Effect of Focused Ion Beam Irradiation on a Self-Assembled Monolayer. J. Phys. Chem. C 2016, 120 (1), 274–280.
- (27) Ada, E. T.; Hanley, L.; Etchin, S.; et al. Ion Beam Modification and Patterning of Organosilane Self-Assembled Monolayers. J. Vac. Sci. Technol., B: Microelectron. Nanometer Struct.—Process., Meas., Phenom. 1995, 13 (6), 2189.
- (28) Rappe, A. K.; Casewit, C. J.; Colwell, K. S.; Goddard, W. A.; Skiff, W. M. UFF, a Full Periodic Table Force Field for Molecular Mechanics and Molecular Dynamics Simulations. *J. Am. Chem. Soc.* 1992, 114 (25), 10024–10035.
- (29) Hu, K.; Luo, L.; Sun, X.; Li, H. Unraveling the Effects of Gas Species and Surface Wettability on the Morphology of Interfacial Nanobubbles. *Nanoscale Adv.* **2022**, *4* (13), 2893–2901.
- (30) Javanbakht, G.; Sedghi, M.; Welch, W.; Goual, L. Molecular Dynamics Simulations of CO ₂ /Water/Quartz Interfacial Properties: Impact of CO ₂ Dissolution in Water. *Langmuir* **2015**, *31* (21), 5812–5819.
- (31) Mehana, M.; Fahes, M.; Huang, L. The Density of Oil/Gas Mixtures: Insights From Molecular Simulations. *SPE J.* **2018**, 23 (5), 1798–1808.

- (32) Zou, Z.-L.; Quan, N.-N.; Wang, X.-Y.; Wang, S.; Zhou, L.-M.; Hu, J.; Zhang, L.-J.; Dong, Y.-M. The Properties of Surface Nanobubbles Formed on Different Substrates. *Chin. Phys. B* **2018**, 27 (8), No. 086803.
- (33) Simonsen, A. C.; Hansen, P. L.; Klösgen, B. Nanobubbles Give Evidence of Incomplete Wetting at a Hydrophobic Interface. *J. Colloid Interface Sci.* **2004**, 273 (1), 291–299.
- (34) Zhang, L.; Zhang, X.; Zhang, Y.; Hu, J.; Fang, H. The Length Scales for Stable Gas Nanobubbles at Liquid/Solid Surfaces. *Soft Matter* **2010**, *6* (18), 4515–4519.
- (35) Lohse, D.; Zhang, X. Surface Nanobubbles and Nanodroplets. *Rev. Mod. Phys.* **2015**, *87* (3), 981–1035.
- (36) Lohse, D.; Zhang, X. Pinning and Gas Oversaturation Imply Stable Single Surface Nanobubbles. *Phys. Rev. E* **2015**, *91* (3), No. 031003.
- (37) An, H.; Tan, B. H.; Zeng, Q.; Ohl, C.-D. Stability of Nanobubbles Formed at the Interface between Cold Water and Hot Highly Oriented Pyrolytic Graphite. *Langmuir* **2016**, 32 (43), 11212–11220.
- (38) Wang, Y.; Li, X.; Ren, S.; Tedros Alem, H.; Yang, L.; Lohse, D. Entrapment of Interfacial Nanobubbles on Nano-Structured Surfaces. *Soft Matter* **2017**, *13* (32), 5381–5388.